




Determination of Source, Site, and Path Effects of Mw = 7.3, 2017 Sarpol-e Zahab Using a Non-Parametric Generalized Inversion Technique

SEYED REZA SAKHAEI,¹ MAJID MAHOOD,²  REZA HEIDARI,¹ and MEHRAN ARIAN¹

Abstract—A nonparametric generalized inversion technique has been used to derive source parameters, attenuation characteristics, and site amplification effects from *S*-wave spectra of the Mw 7.3 Sarpol-e Zahab, November 12, 2017 aftershocks recorded at 13 stations in the hypocentral distance of 9–70 km. We used a total number of 87 Fourier amplitude spectra from 30 aftershocks with ML 3.8–5.3 in the frequency range 0.5–25 Hz. The inverted source spectra fitted with the omega-square source model and obtained some of the source parameters. The estimated stress drop varies from 0.98 to 30.18 MPa, which is compatible with values of the stress drop for crustal earthquakes in other regions. There is a linear correlation between the moment magnitude Mw and the local magnitude ML as $M_w = 0.71 ML + 1.27$. This equation is close to the other relationships obtained for the Zagros region in the previous studies. The seismic moment and the cube of corner frequency are inversely related to each other as $M_0 f_c^3 = 3 \times 10^{16}$. The obtained nonparametric attenuation functions are curves that decay almost uniformly and slowly with distance for all frequencies. The quality factor is estimated as $Q = 107.75 f^{0.87}$. The value of Q_0 is small and the power of the frequency is close to 1, which is characteristic of an active tectonic environment. The site effects obtained from generalized inversion and the H/V method were compared, and it was observed that both results were almost the same.

Keyword: Generalized inversion, source parameter, attenuation function, site effect, Zagros.

1. Introduction

The Zagros Fold and Thrust Belt, known as one of the youngest and most active continental collision zones on Earth, is the result of the continued convergence between the Arabia and Eurasia plates (Snyder & Barazangi, 1986). The Zagros is located in

the south and southwest of Iran, where a relatively large population is involved in tectonic events and activities. This region has three main faults: the Zagros Main Recent Fault (ZMRF), the High Zagros Fault (HZF), and the Zagros Mountain Front Fault (ZMFF). Most earthquakes are small, medium, and shallow. Of course, there have been a few exceptions. The most devastating earthquake of the Zagros occurred on January 23, 1909, with mb = 7.4, and produced over 40 km surface rupture (Tchalenko & Braud, 1974). Also, an unexpected and devastating earthquake occurred on November 12, 2017, with Mw = 7.3, in the west of Zagros (Sarpol-e Zahab near the Iran-Iraq border). Therefore, it is important to identify the various aspects of these events, including determining the effects of source, path, and site. According to the National Center of Broadband Seismic Network of Iran, the epicenter of this event was located at 34.88° N and 45.84° E, with a depth of 23 km (Fig. 1). Several studies indicate that this earthquake occurred on a shallow northeast dipping fault plane (e.g., Gombert et al., 2019; Durmus & Utkucu, 2021).

In this study, the effects of source, path, and site of the 2017 Sarpol-e Zahab earthquake were estimated using the generalized inversion technique (GIT). This method was first proposed by Andrews (1986) by recasting the method of spectral ratios into a generalized inverse problem. Other researchers used and developed this method (e.g., Boatwright et al., 1991; Castro et al., 1990; Hartzell, 1992; Oth et al., 2008, 2011; Parolai et al., 2000; Salazar et al., 2007). To achieve this, appropriate records of aftershocks were selected and their shear wave spectra were extracted for inversion. After determining the source spectrum, corner frequency and seismic

¹ Department of Earth Sciences, Science and Research Branch, Islamic Azad University, Tehran, Iran.

² International Institute of Earthquake Engineering and Seismology (IIEES), Tehran, Iran. E-mail: m.mahood@iiees.ac.ir

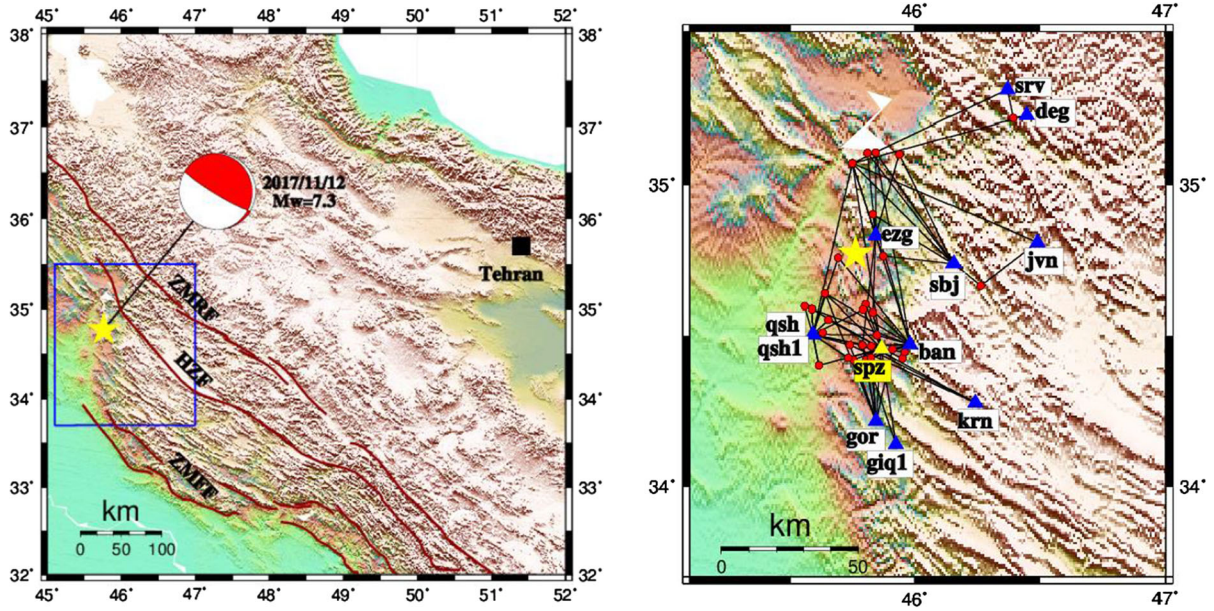


Figure 1

Left: Three major reverse faults in the Zagros region: ZMRF (Zagros Main Recent Fault), HZF (High Zagros fault), ZMFF (Zagros Mountain Front Fault). Also, the location of the main earthquake in Sarpol-e Zahab along with its focal mechanism is shown. Right: Magnified image of the blue box on the left; red circles: aftershocks, blue triangles: stations (the reference station is highlighted), black lines: records ray paths

moments were also estimated using the ω^2 -model (Brune, 1970, 1971). Also, seismic energy was determined, and after determining the moment magnitude, its relationship with the local magnitude was obtained. By determining the attenuation spectra, the best model for the quality factor of the area was obtained and compared with other studies. Finally, the structural effects were estimated and the results were compared by the horizontal-to-vertical spectral ratio (H/V) method.

2. Dataset

In order to perform inversion, the data of the accelerometer network of the Building and Housing Research Center (BHRC) were used. These data are related to the 2017 $M_w = 7.3$ Sarpol-e Zahab earthquake aftershocks, from which appropriate data were selected. The criteria for selecting the data included good signal-to-noise ratio ($\text{SNR}(f) > 3$), appropriate distance, recording of each event by at least two stations, recording of at least two events by each

station, and so on. Based on these conditions, 87 records were selected from the available data (black line on Fig. 1). These records, which were recorded in 13 stations (Table 1), are related to 30 aftershocks (Table 2). Most records were recorded by stations ban

Table 1

The accelerometer stations used in this study

ID	Name	Record number	Longitude (°)	Latitude (°)	Elevation (m)	V_{s30} (m/s)
1	gor	9	45.845	34.218	663	403
2	spz	14	45.868	34.459	558	619
3	spz1	5	45.868	34.459	558	619
4	ban	15	45.982	34.473	1009	–
5	km	3	46.24	34.279	1562	800
6	qsh	11	45.591	34.506	395	340
7	qsh1	7	45.591	34.506	395	340
8	deg	2	46.447	35.226	1295	–
9	srv	2	46.369	35.311	1025	–
10	ezg	8	45.843	34.832	710	–
11	sbj	7	46.154	34.738	1248	281
12	giq1	2	45.925	34.14	830	692
13	jvn	2	46.489	34.809	1340	298

V_{s30} was not available for some stations. V_{s30} is reported by BHRC

Table 2
The aftershocks used in this study

Event ID	Origin time		Lon (°)	Lat (°)	Depth (km)	ML
	yy/mm/dd	hh:mm:ss				
1	17/11/12	20:42:45	45.865	34.466	8.0	4
2	17/11/12	21:33:22	45.803	34.605	8.0	4.5
3	17/11/13	04:27:55	45.804	34.421	10.0	4.8
4	17/11/13	04:36:12	45.824	34.428	10.0	4.3
5	17/11/13	09:19:28	45.755	34.421	8.0	4.7
6	17/11/13	13:12:37	45.74	34.471	8.0	4.5
7	17/11/14	01:08:45	45.911	34.457	8.0	4.1
8	17/11/15	07:11:19	45.849	34.504	8.0	4
9	17/11/15	15:20:37	45.588	34.589	9.5	4.2
10	17/11/16	00:16:15	45.615	34.403	9.3	3.8
11	17/11/16	01:09:19	45.558	34.598	8.0	3.8
12	17/11/18	04:12:15	45.631	34.512	13.0	4.5
13	17/11/19	01:07:33	45.96	34.447	8.0	4.1
14	17/11/19	02:59:15	45.951	34.426	10.0	3.9
15	17/11/19	06:19:48	46.392	35.218	8.5	4.2
16	17/11/20	15:36:00	45.832	34.901	12.0	4.3
17	17/11/21	17:46:19	45.653	34.554	10.0	4
18	17/11/22	20:34:03	45.693	34.758	10.0	4.2
19	17/11/26	05:47:31	45.832	34.578	15.0	4.4
20	17/12/06	05:53:43	45.81	35.105	8.0	4.8
21	17/12/06	07:57:41	45.64	34.64	8.0	4.7
22	17/12/08	01:55:00	45.938	35.1	10.0	4.3
23	17/12/08	07:39:43	45.733	34.428	5.8	4.2
24	17/12/11	14:09:56	45.75	35.07	20.0	5.3
25	17/12/11	14:42:40	45.844	35.106	10.0	4.9
26	17/12/19	09:15:47	45.874	34.764	7.7	4.2
27	17/12/20	20:01:06	45.826	34.467	8.0	4.5
28	17/12/20	20:22:06	46.262	34.665	6.0	4.6
29	17/12/21	02:50:14	45.793	34.588	12.0	4.4
30	18/01/06	15:22:07	45.79	34.47	14.0	5

and spz, with 15 and 14 data points, respectively. The magnitude range of ML is from 3.8 to 5.3 and the hypocentral distance range is from 9 to 70 km (Fig. 2). Of course, records with larger hypocentral distances were also available, but due to the low density of records at distances larger than 70 km, they were not selected for inversion.

First, a baseline correction and a Butterworth band-pass filter (from 0.2 to 30 Hz) were applied to each record. Since the major portion of the seismic energy is generated in the form of S-waves, the analysis should be performed on this part of the strong motion records (Zafarani et al., 2012). Husid's method (Husid, 1967) was used to select the start

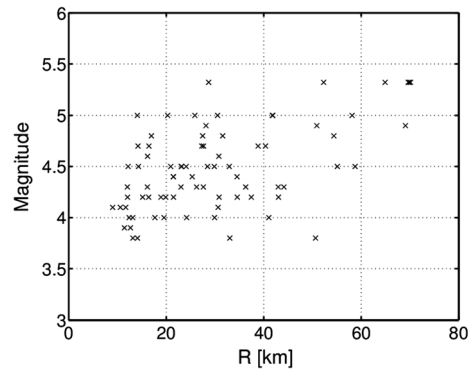


Figure 2
Distribution of magnitude (ML) versus hypocentral distance

time of the S-wave (t_0) when the record energy reaches 5% of the total wave energy. Kinoshita's method (Kinoshita, 1994) was also used to select the end time of the S-wave (t_1). Kinoshita (1994) defined the acceleration envelop function [$e(n)$] and the cumulative acceleration function [$c(k)$] according to the following equations:

$$e(n) = (a^2(n) + H^2\{a(n)\})^{1/2} \quad (1)$$

$$c(k) = \left(k^{-1} \sum_{n=1}^k e^2(n) \right)^{1/2} \quad (2)$$

In this relationship, a is the record of acceleration and H is the Hilbert transform. In this method, the end time of the S-wave is equal to the time at which the cumulative envelope function begins to decline (following the strategy of Kinoshita, 1994). In the next step, the Fourier spectrum of the S-wave must be calculated. However, the sudden interruption of the wave has a great impact on the Fourier spectrum. Therefore, after selecting the time of the beginning and end of the S-wave, a cosine taper was applied to it.

The abovementioned steps should be done for both horizontal components, and then the root mean square of both horizontal components should be calculated. Due to sudden changes in the Fourier spectrum, a smoothing function must be applied to it. One of the suitable methods for this work is the method of Konno and Ohmachi (1998). In this method, a window is applied to the signals according to the following equation:

$$W(f, f_c) = \left[\frac{\sin\left(\log\left(\frac{f}{f_c}\right)^b\right)}{\log\left(\frac{f}{f_c}\right)^b} \right]^4 \quad (3)$$

where f' represents the central frequency around which the smoothing is performed and supposed $b = 20$. This window has constant width on the logarithmic frequency axis. The frequency range in this study is 0.5–25 Hz, from which the values of the acceleration spectrum at 40 points with the same logarithmic distances are interpolated from this range.

3. Generalized Inversion Technique

The generalized inversion technique is based on the ground motion convolution model (multiplication in the frequency domain):

$$U_{ij}(f, R) = S_i(f) \cdot P(f, R) \cdot I_j(f) \quad (4)$$

In this formula, $U_{ij}(f, R)$ is the Fourier amplitude spectrum (in this study, the horizontal component of the observed acceleration) from the i th source and the j th station at the hypocentral distance R . Also, $S_i(f)$ is the source function, $P(f, R)$ is the attenuation function along the path, and $I_j(f)$ is the local amplification of the site. By applying logarithms to both sides of this equation, the problem becomes linear:

$$\log U_{ij}(f, R) = \log S_i(f) + \log P(f, R) + \log I_j(f) \quad (5)$$

If we have N records, the above equation will become a system of linear equations with N relation ($Ax = b$). Like most geophysical problems, it is overdetermined. Therefore, by choosing an appropriate approach to inversion such as singular value decomposition (SVD) (Menke, 1989) we will have:

$$x = (A^T A)^{-1} A^T b \quad (6)$$

These steps were first described by Andrews (1986). He worked on data with low hypocentral distance, as well as data from which the effect of geometric spreading had been removed. If we have a suitable attenuation model (geometric distribution, quality factor, etc.) from other studies, and NE is the

number of sources (events) and NS is the number of sites (stations), the number of unknowns will be $NS + NE$. The unknowns will be calculated at each frequency separately. The coefficient matrix will consist of zeros and ones only. In other studies such as Hartzell (1992), Hartzell et al. (1996), and Parolai et al. (2001), the effects of the attenuation function on the records were also corrected.

As Andrews (1986) and other researchers have pointed out, there is a degree of freedom in relation (5), so that by multiplying one number in each sentence and dividing the same number in another sentence, there will be no change in the acceleration spectrum. This can also be problematic in the SVD method, with zero singular values for the coefficient matrix. To prevent this, we can consider a default value for the source (e.g., Salazar et al., 2007) or site. A common assumption for the site is that the site response (I) in rock sites is independent of frequency, and its value is considered to be 1 (e.g., Hartzell, 1992; Hartzell et al., 1996; Parolai et al., 2000).

4. Results

4.1. Source Effect

One of the unknowns in the inversion procedure is the effect of the seismic source, which is obtained as a spectrum for each source (event). Since 30 events were considered in the present study, 30 spectra of the source are obtained in this section. For example, four source spectra are shown in Fig. 3. The spectrum obtained from generalized inversion is marked with a full line, and its standard deviation is marked with a gray color (shadow). Also, the origin time of each event and its depth and moment magnitude are written on each spectrum.

From the source spectra, we can have an analysis of other parameters such as seismic moment (M_0), corner frequency (f_c), and stress drop ($\Delta\sigma$). Based on the ω^2 source model (Brune, 1970, 1971) we will have:

$$S(f) = (2\pi f)^2 \cdot \frac{R_{\theta\phi} V F}{4\pi\rho_s \beta_s^3 R_0} \cdot \frac{M_0}{1 + (f/f_c)^2} \quad (7)$$

where $R_{\theta\phi} = 0.55$ is the mean value of the S -wave

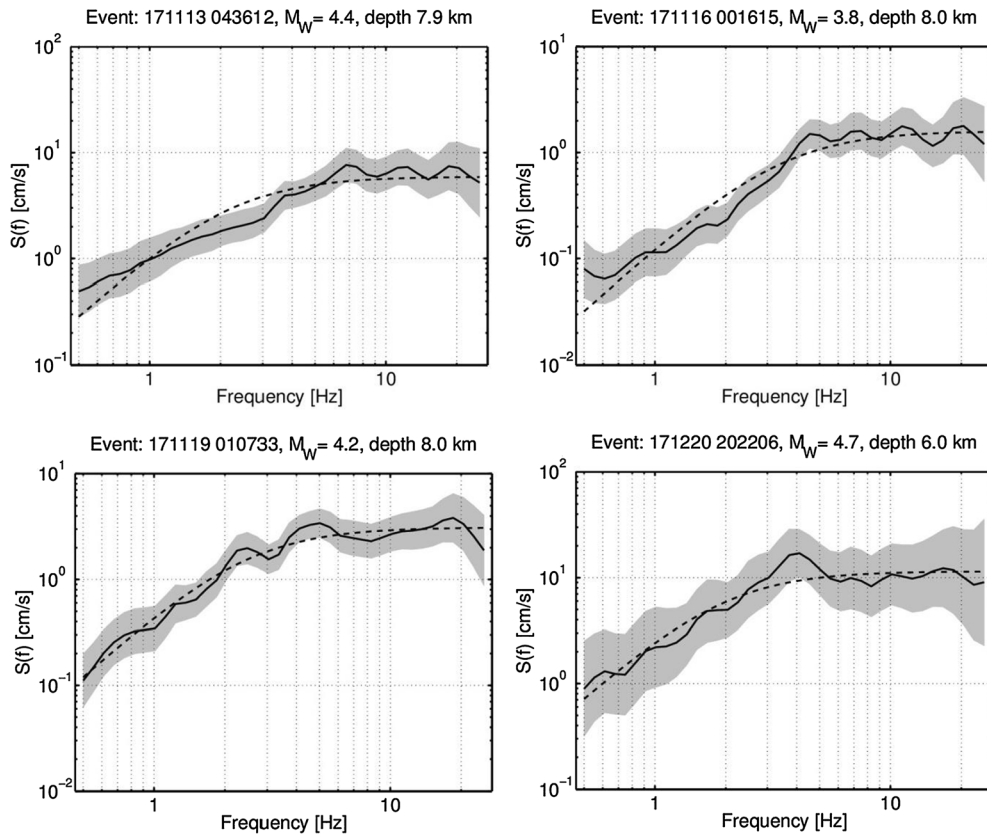


Figure 3
The source spectrum of four events obtained by GIT

radiation pattern, and the value of $V = 1/\sqrt{2}$ is considered to include the ratio of the division of the total energy into two horizontal components. $F = 2$ is free surface amplification. $\rho_s = 2800 \text{ gr/cm}^3$ and $\beta_s = 3.7 \text{ km/s}$ are considered as the average for the path density and velocity of the S -waves, respectively. Corner frequency and seismic moment are our unknowns that will be obtained using nonlinear regression. By placing these two parameters in the source equation, the theoretical source spectrum is obtained (dashed lines in Fig. 3). The logarithmic diagram of the corner frequency in terms of the seismic moment is shown in Fig. 4a. Other quantities called source radius (r) and stress drop ($\Delta\sigma$) in this source model are defined as follows:

$$r = \frac{2.34\beta_s}{2\pi f_c}$$

$$\Delta\sigma = \frac{7M_0}{16r^3} \quad (8)$$

In order to determine the moment magnitude (M_w) based on the seismic moment, the equation of Hanks and Kanamori (1979) has been used:

$$\log M_0 = 1.5M_w + 9.05 \quad (9)$$

The diagram of M_w versus local magnitude (ML) is shown in Fig. 4(b). The M_w range is obtained from 3.8 to 5.2. The best-fitted line for this diagram is estimated to be $M_w = 0.71 \text{ ML} + 1.27$, and its regression coefficient was $R^2 = 0.73$.

Also, the apparent stress σ_a can be calculated by $\sigma_a = \mu E_s/M_0$, where μ and E_s are the rigidity modulus ($\mu = \rho_s \beta_s^2$) and the radiated energy of the S -wave, respectively. In this study, the equation of Izutani and Kanamori (2001) is used to estimate the energy:

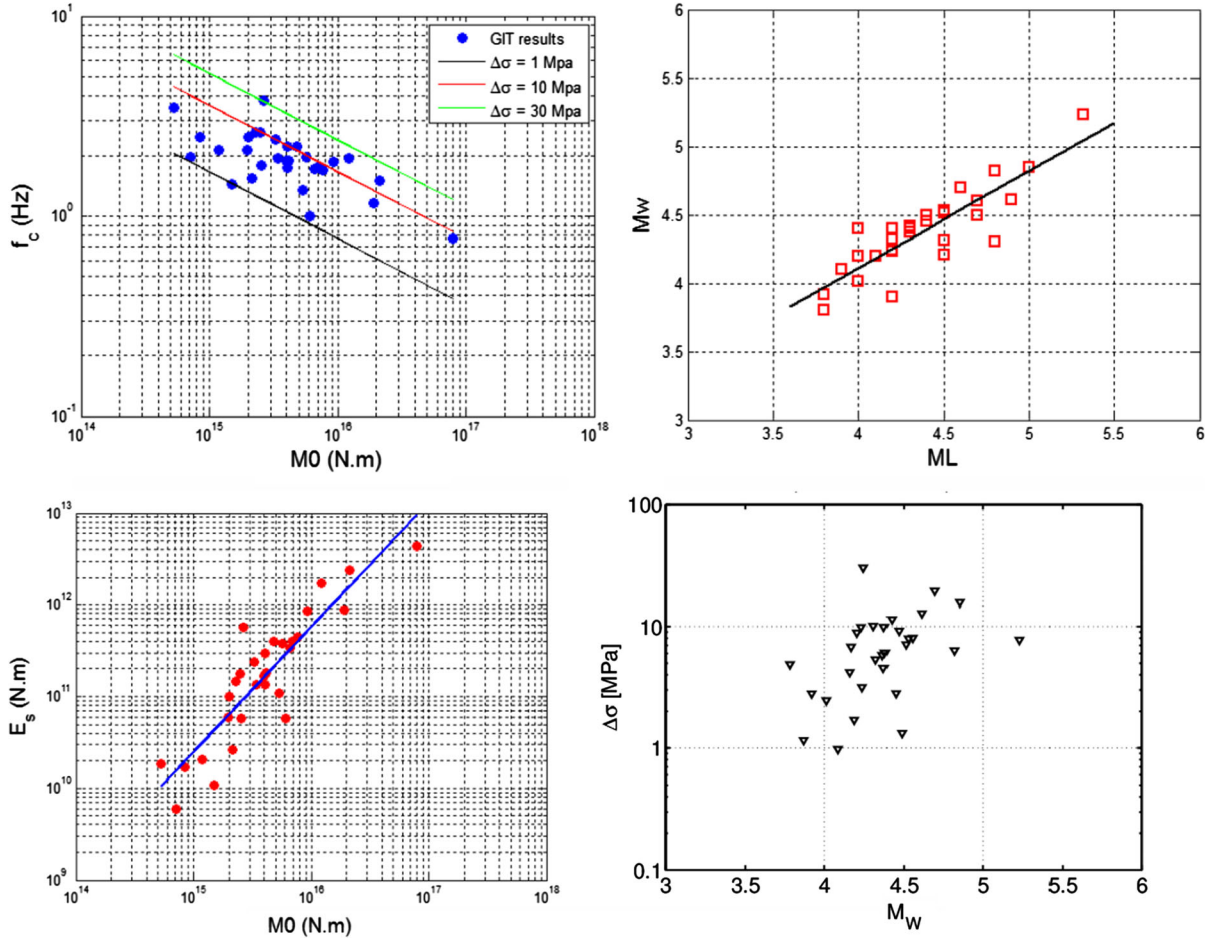


Figure 4

a Corner frequency (f_c) versus seismic moment (M_0). The relationship between f_c and M_0 for three various constant stress drops (1, 10, and 30 Mpa) is represented by solid lines. These lines come from Eq. 8. **b** M_w obtained in this study versus M_L reported by the ISC catalog, along with the best-fitted line. **c** Radiated energy (E_s) versus seismic moment along with the best-fitted line. **d** the scatter diagram of stress drop versus moment magnitude

$$E_s = \frac{4\pi}{5\rho_s\beta_s^5} \int_0^{\infty} \left| \frac{fM_0}{1 + \left(\frac{f}{f_c}\right)^2} \right|^2 df \quad (10)$$

These parameters for all 30 sources are shown in Table 3. The corner frequencies vary from 0.8 to 3.8 Hz. The minimum and maximum seismic moments are 5.3×10^{14} and 7.9×10^{16} N m, respectively. As shown in Fig. 4a, the corner frequency decreases as the magnitude of the earthquake increases. Seismic moment and the cube of corner frequency are inversely related to each other, so we can write: $M_0 f_c^3 = \text{constant}$. In this study, the

constant is equal to $3 \times 10^{16} \text{ N m s}^{-3}$. In other words, $\log M_0 = 16.48 - 3 \log f_c$ with regression coefficient 0.80. The ranges of stress drop and apparent stress are from 0.98 to 30.18 MPa and from 0.23 to 7.03 MPa, respectively. The relationship between these two parameters is estimated as $\Delta\sigma = 4.29\sigma_a$ with a regression coefficient of 0.99. In this study, no significant relationship was observed between stress drop (or apparent stress) and moment magnitude (or seismic moment). This can also be seen in Fig. 4d. The S-wave radiated energy varies from 5.96×10^9 to 4.41×10^{12} J. It is clear that energy is directly related to the magnitude of the earthquake (or seismic

Table 3

Some of the source parameters obtained in this study such as corner frequency (f_c), seismic moment (M_0), moment magnitude (M_w), source radius (r), stress drop ($\Delta\sigma$), apparent stress (σ_a), and radiated S-wave energy (E_s)

Event ID	f_c (Hz)	M_0 (N m)	M_w	R (m)	$\Delta\sigma$ (Mpa)	σ_a (Mpa)	E_s (J)
1	1.9	4.2E+15	4.4	669.76	6.10	1.42	1.83E+11
2	1.7	7.0E+15	4.5	725.61	7.98	1.86	4.00E+11
3	3.8	2.6E+15	4.2	336.66	30.18	7.03	5.71E+11
4	2.2	4.9E+15	4.4	569.92	11.49	2.68	4.02E+11
5	1.7	7.6E+15	4.6	745.51	8.08	1.88	4.45E+11
6	1.7	6.6E+15	4.5	740.10	7.14	1.66	3.40E+11
7	2.2	2.0E+15	4.2	588.94	4.20	0.98	5.93E+10
8	1.5	2.2E+15	4.2	821.36	1.71	0.40	2.65E+10
9	1.9	3.4E+15	4.3	654.93	5.37	1.25	1.33E+11
10	3.5	5.3E+14	3.8	362.14	4.88	1.14	1.86E+10
11	2.5	8.5E+14	3.9	510.85	2.80	0.65	1.72E+10
12	2.6	2.3E+15	4.2	482.65	8.92	2.08	1.47E+11
13	2.5	2.0E+15	4.2	506.70	6.80	1.58	9.88E+10
14	1.4	1.5E+15	4.1	878.07	0.98	0.23	1.06E+10
15	2.0	7.1E+14	3.9	645.78	1.16	0.27	5.96E+09
16	1.9	4.0E+15	4.4	668.70	5.83	1.36	1.67E+11
17	2.1	1.2E+15	4.0	593.82	2.46	0.57	2.07E+10
18	2.6	2.5E+15	4.2	480.42	9.90	2.31	1.79E+11
19	1.0	6.0E+15	4.5	1259.26	1.32	0.31	5.76E+10
20	1.2	1.9E+16	4.8	1094.44	6.36	1.48	8.71E+11
21	2.0	5.7E+15	4.5	645.66	9.23	2.15	3.77E+11
22	2.2	4.1E+15	4.4	564.93	9.96	2.32	2.94E+11
23	1.7	4.1E+15	4.4	730.71	4.57	1.06	1.34E+11
24	0.8	7.9E+16	5.2	1644.56	7.77	1.81	4.41E+12
25	1.9	9.3E+15	4.6	682.58	12.85	2.99	8.63E+11
26	1.8	2.6E+15	4.2	707.91	3.16	0.74	5.82E+10
27	2.4	3.3E+15	4.3	521.01	10.13	2.36	2.38E+11
28	1.9	1.2E+16	4.7	651.92	19.51	4.55	1.73E+12
29	1.4	5.3E+15	4.4	937.61	2.82	0.66	1.07E+11
30	1.5	2.1E+16	4.9	841.53	15.74	3.67	2.43E+12

Table 4

Some of the relationships between M_w and M_L considered in this paper

Number	Equation	Region	References
1	$M_w = 0.67 M_L + 1.62$	Zagros	Karimiparidari et al., (2013)
2	$M_w = 0.74 M_L + 1.35$	Zagros	Shahvar et al., (2013)
3	$M_w = 0.81 M_L + 1.10$	Zagros	Mousavi-bafrouei et al., (2014)
4	$M_w = 1.01 M_L - 0.05$	Zagros	Zare et al., (2014)
5	$M_w = 0.68 M_L + 0.91$	Parts of Zagros	Ahmadzadeh et al., (2017)

moment) (Fig. 4b), so that in this study the relationship between them is as follows (with regression coefficient $R^2 = 0.79$):

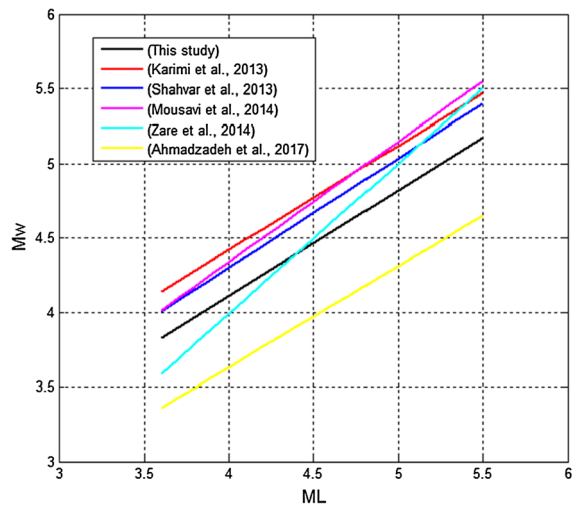


Figure 5

Comparison of the relationship between moment magnitude and local magnitude obtained in this study and the results of other studies

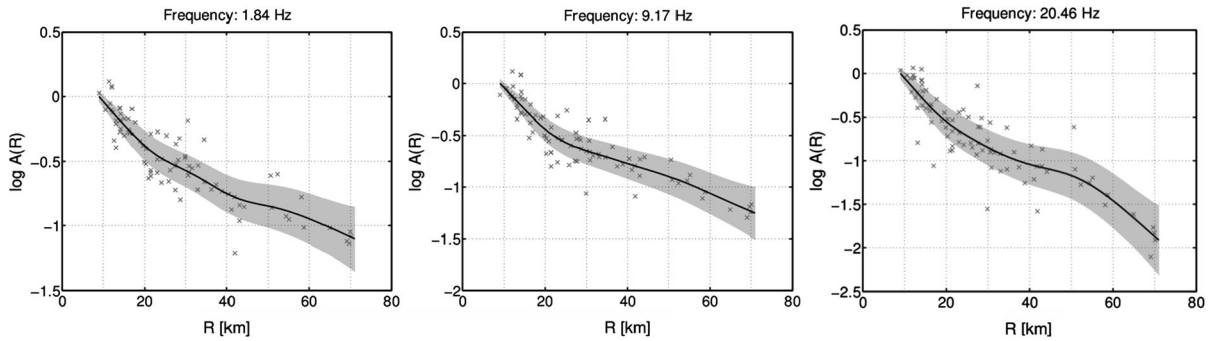


Figure 6

The attenuation spectra versus hypocentral distance in three selected frequencies. The gray crosses and shaded area represent the attenuation and the standard deviation around the mean, respectively

$$\log E_s = 1.37 \log M_0 - 10.09 \quad (11)$$

As mentioned, the relationship between moment magnitude and local magnitude is estimated as $M_w = 0.71 ML + 1.27$. In order to compare this relationship with previous studies, five relationships were considered (Table 4):

The relationship obtained in this study agrees well with other relationships, especially with the relationship of Zare et al. (2014) and Shahvar et al. (2013), which has the least differences with them. In order to better represent and compare these relationships, their diagrams for the local magnitude range 3.6–5.5 are shown in Fig. 5.

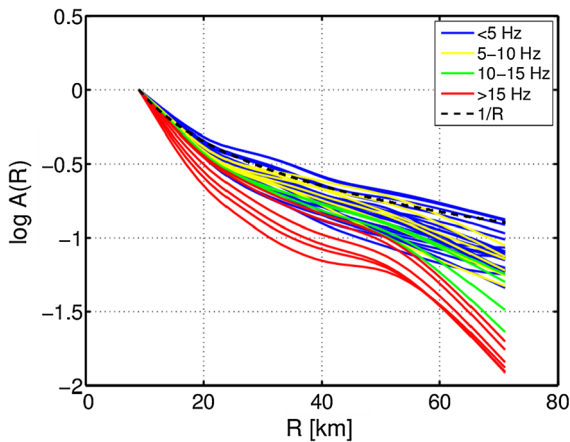


Figure 7

Attenuation spectra versus hypocentral distance for all frequencies

4.2. Attenuation Effect

One of the results of inversion is nonparametric attenuation functions, which are estimated at different frequencies. For example, Fig. 6 shows three attenuation functions at frequencies of 1.84, 9.17, and 20.46. As can be seen, the attenuation function changes smoothly and decreases with increasing distance. In order to better understand the attenuation function curve, its variations in all 40 selected frequencies along with curve $1/R$ are shown in Fig. 7. Due to the choice of $R_0 = 9$ km as the reference distance, the $\log(A, R)$ in this distance is zero.

Considering the attenuation equation (Boore, 2003):

$$A(f, R) = \left(\frac{R_0}{R}\right)^b \exp\left(\frac{-\pi f}{Q(f) \cdot \beta} (R - R_0)\right) \quad (12)$$

in this study, $\left(\frac{R_0}{R}\right)^b$ is a simple model of geometrical spreading, where b is the geometrical spreading component. By applying the logarithm to the sides of Eq. (12) and arranging its sentences we will have:

$$\log A(f, R) - \log\left(\frac{R_0}{R}\right)^b = \frac{-\pi f}{Q(f) \cdot \beta} (R - R_0) \quad (13)$$

According to the necessary condition of $\log A(f, R) - \log\left(\frac{R_0}{R}\right)^b < 0$, we seek out a maximum b to meet this condition for each frequency, indicating the strongest geometrical spreading (Wang et al., 2018). By drawing the diagram to the left of Eq. 13 versus distance (for each frequency) and calculating

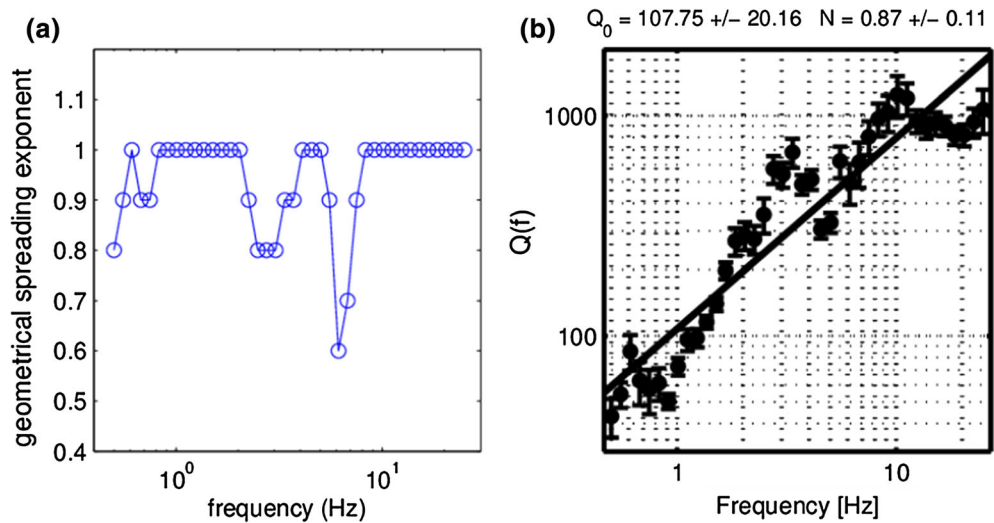


Figure 8

a The geometrical spreading exponent for all frequencies. **b** The Q values at each frequency (0.5–25 Hz) along with their error bars. The solid line represents the best-fitted Q -model for this study

the slope, the Q factor will be determined. On the other hand, we considered an additional condition (in addition to the above condition) so that by selecting it, the regression coefficient of Eq. (13) becomes at least 0.80. Values of 0.6 to 1 were tested for all frequencies, and the appropriate value is shown in Fig. 8a. As can be seen, in most frequencies the values 1 and 0.9 were selected, and only a few of them are 0.8 and 0.7. The values of Q at different

frequencies are shown in Fig. 8b. A line ($Q = Q_0 f^N$) was traditionally fitted to it. In this study, the quality factor was estimated as $78 f^{0.98}$ by the least-square solution. The value of Q_0 is small, and the power of the frequency is close to 1, which is characteristic of an active tectonic environment.

4.3. Site Response

As mentioned, in order to eliminate the degree of freedom of Eq. 5, the response of the rock site can be considered equal to 1 (independent of frequency). In this study, because the type of sites is unknown, previous studies have been used. Boore and Joyner (1997) estimated the site response with $V_{s30} = 620$ m/s (Fig. 9). According to Table 1, among our sites, the spz station has $V_{s30} = 619$ m/s. Therefore, the site response of the spz station was assumed to be known (i.e., equal to the values obtained by Boor and Joyner (1997) for $V_{s30} = 620$ m/s).

The horizontal-to-vertical spectral ratio technique (the H/V or HVSR method), introduced by Lermo and Chavez-Garcia (1993), indicates some effects of the site (mainly the fundamental frequency, if it exists). This method has been widely used by various researchers. In this method, it is assumed that the local effects of the site do not have a significant effect

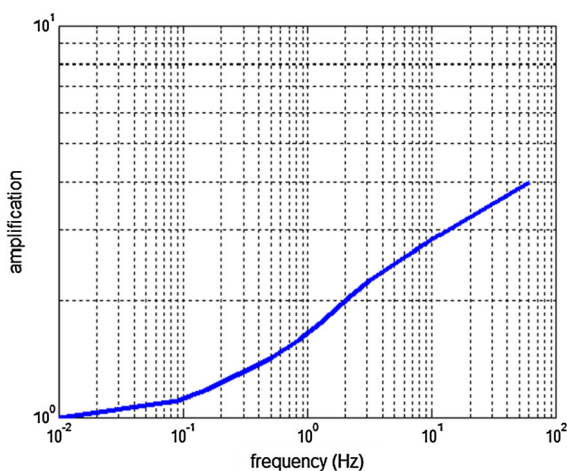


Figure 9

The site amplification diagram for sites with $V_{s30} = 620$ m/s (Boore & Joyner, 1997)

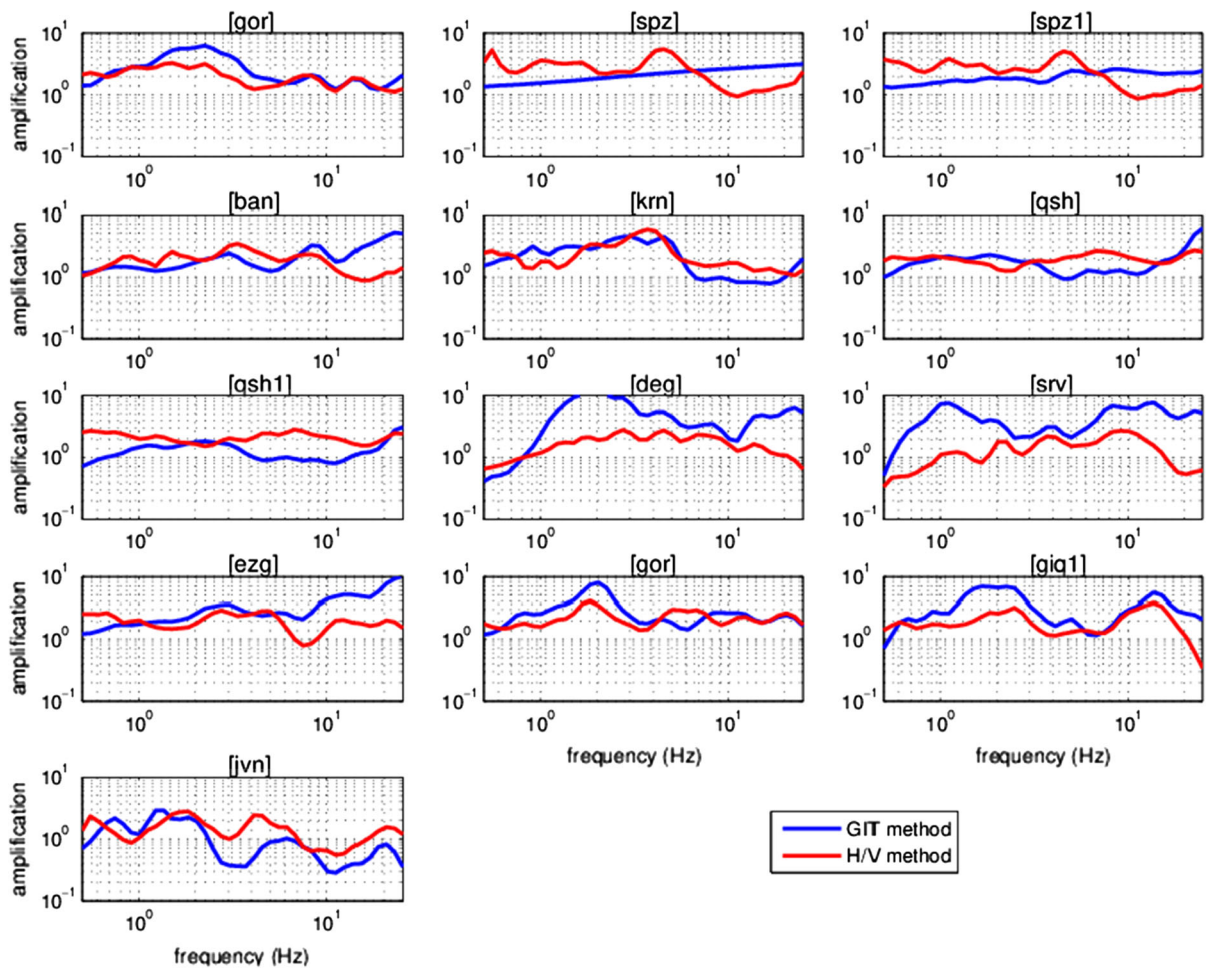


Figure 10
The site response of S-waves obtained by the GIT in this study and the corresponding S-wave HVSR

on the vertical component records. In this section, the effects of the site obtained from GIT and the H/V method were compared. The diagrams of site amplification from GIT (blue line) and the H/V method (red line) in the frequency range of 0.5–25 Hz is shown in Fig. 10.

4.4. Residuals Distribution

In order to evaluate the stability and accuracy of the inversion results, first, the residuals from the synthetic results (generated by GIT) and observations were calculated at each frequency. For example, the residual diagrams in three frequencies of 2.04, 8.29, and 18.50 are shown in Fig. 11 (first row). This

diagram is plotted in terms of hypocentral distance. Given the small amount of residual and also the independence of the distance, it can be concluded that the results of the inversion are reliable and close to reality. In the next step, values of 1 to 10% of the observations were added to or subtracted from them (randomly). These changes were made in the observations to firstly assess the sensitivity of the inversion to the input data and secondly not to claim that the input data is 100% correct. GIT was then applied to these modified data, and no significant changes appeared in the results, so that the remaining values have changed slightly (Fig. 11, second row). Since the differences of the two residuals are not noticeable, in order to better understand the values of the

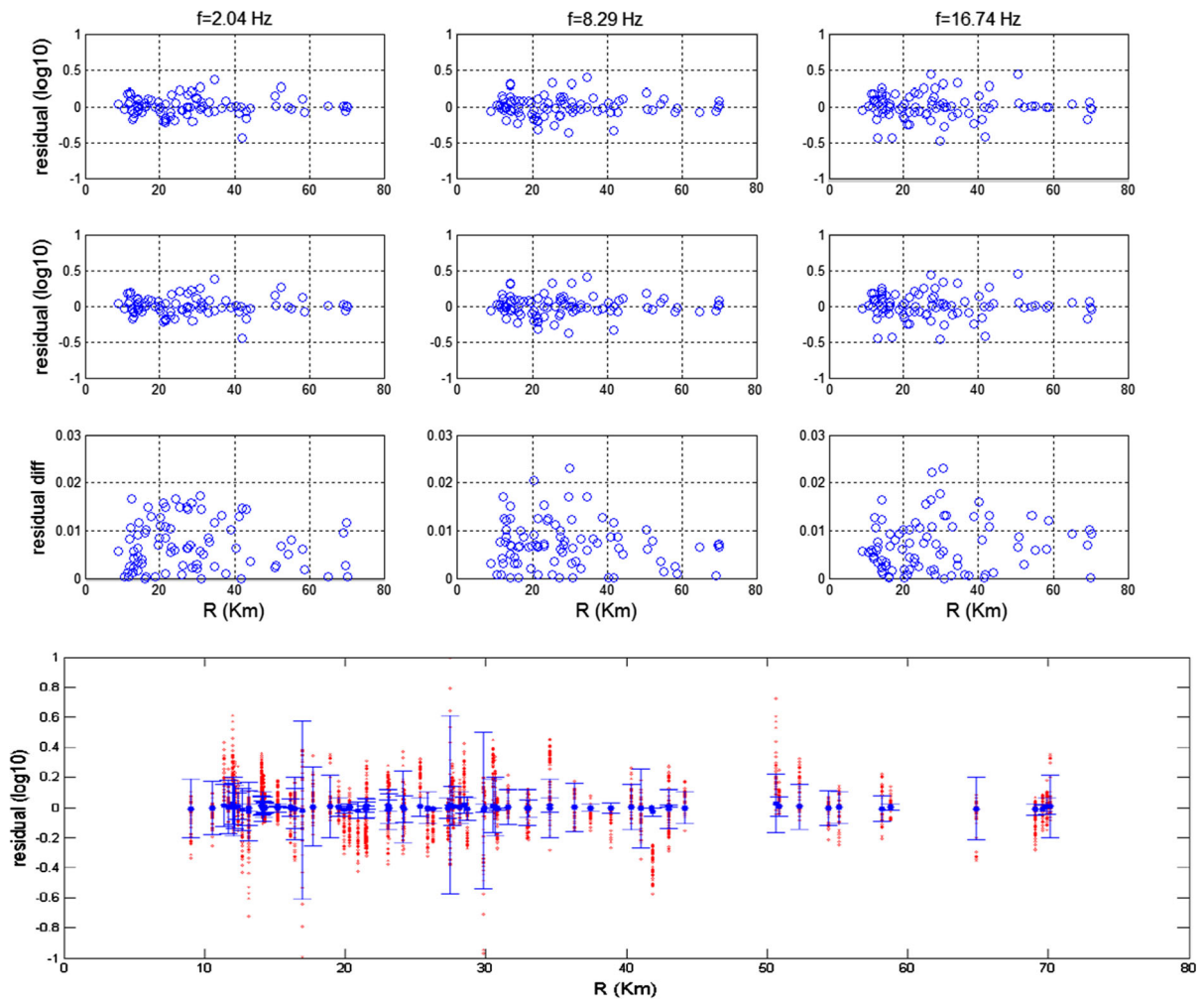


Figure 11

Top: residual diagram of GIT for three frequencies ($f = 2.04$ Hz [first column], $f = 8.29$ Hz [second column] and $f = 16.74$ Hz [third column]). First row: residual with main observed data, second row: residual with changed observed data, third row: differences between first and second rows. Bottom: all the residuals of all the frequencies together in a plot (red dot) vs the hypocentral distance, and the average value (blue dot) and the corresponding standard deviation

differences, a diagram of the difference between them is also drawn (Fig. 11, third row).

5. Discussion and Conclusion

The source, attenuation, and site parameters of the 2017 Sarpol-e Zahab aftershocks were investigated using the non-parametric generalized inversion method. Eighty-seven acceleration records were selected from 30 sources for inversion.

The range of the corner frequency and the seismic moment varies from 0.8 to 3.8 Hz and from 5.3×10^{14} to 7.9×10^{16} N.m, respectively. This range is consistent with other studies. For example, Zafarani et al. (2012) estimated the corner frequency of Alborz as a range of 0.05–4 Hz. Their data ranged in moment magnitude from 4 to 7.4 and seismic moment from 1.26×10^{15} to 1.41×10^{20} N.m. The ranges of stress drop and apparent stress are estimated from 0.98 to 30.18 MPa and from 0.23 to 7.03 MPa, respectively. We also suggested a relationship

between moment and local magnitude as $M_w = 0.71 ML + 1.27$ for study area.

The attenuation curve decays almost uniformly with increasing distance. The decay rate is higher for higher frequencies than for lower frequencies. At most frequencies, this curve decays faster than $1/R$. Also, the relationship of the quality factor for this region is estimated as $Q = 78 f^{0.98}$.

We compared the site effects calculated from the GIT with the HVSR computed from the same S-wave dataset. In most cases, relatively good agreement between them regarding the estimation of the fundamental frequencies and the general average amplification at all the sites was observed. The small difference between them is mainly due to the constraints and assumptions of these two methods, because in the H/V method, the site effects on the vertical component are completely eliminated, and on the other hand in the GIT, the site effects for the reference station (in this study spz) are default values.

The successful applicability of the GIT implementation in this study is supported by (i) the good agreement of the source factors with those obtained by the other mentioned studies; (ii) the relative good agreement of the site characteristics with those retrieved by the HVSR, also presented in this study; and (iii) the relatively low standard deviation of the residuals.

Acknowledgements

We thank the Road, Housing and Urban Development Research Center of Iran for providing accelerometric data. The authors also feel the need to thank Dr. Adrien Oth for advice and guidance on inversion codes in the Matlab software. We also appreciate the anonymous reviewers whose good comments and suggestions improved our paper.

Publisher's Note Springer Nature remains neutral with regard to jurisdictional claims in published maps and institutional affiliations.

REFERENCES

- Ahmadzadeh, S., Parolai, S., Javan-Doloei, G., & Oth, A. (2017). Attenuation characteristics, source parameters and site effects from inversion of S waves of the March 31, 2006 Silakhor aftershocks. *Annals of Geophysics*, 60(Suppl. to 6).
- Andrews, D. J. (1986). Objective determination of source parameters and similarity of earthquakes of different sizes. In S. Das, J. Boatwright, & C. H. Scholz (Eds.), *Earthquake source mechanics* (pp. 259–268). AGU.
- Boatwright, J., Fletcher, J., & Fumal, T. (1991). A general inversion scheme for source, site, and propagation characteristics using multiply recorded sets of moderate-sized earthquakes. *Bulletin of the Seismological Society of America*, 81, 1764–1782.
- Boore, D. M. (2003). Simulation of ground motion using the stochastic method. *Pure and Applied Geophysics*, 160(3), 635–676.
- Boore, D. M., & Joyner, W. B. (1997). Site amplifications for generic rock sites. *Bulletin of the Seismological Society of America*, 87, 327–341.
- Brune, J. N. (1970). Tectonic stress and the spectra of seismic shear waves from earthquakes. *Journal of Geophysical Research*, 75, 4997–5009.
- Brune, J. N. (1971). Correction. *Journal of Geophysical Research*, 76, 5002.
- Castro, R. R., Anderson, J. G., & Singh, S. K. (1990). Site response, attenuation and source spectra of Swaves along the Guerrero, Mexico, subduction zone. *Bulletin of the Seismological Society of America*, 80, 1481–1503.
- Durmuş, H., & Utkucu, M. (2021). Coseismic slip distributions and stress interactions of the November 12, 2017, Sarpole-Zahab (Western Iran) earthquake (MW= 7.3) and its aftershocks: seismotectonic implications. *Arabian Journal of Geosciences*, 14(12), 1–21.
- Gombert, B., Duputel, Z., Shabani, E., Rivera, L., Jolivet, R., & Hollingsworth, J. (2019). Impulsive source of the 2017 Mw = 7.3 Ezgeleh, Iran, earthquake. *Geophysical Research Letters*, 46(10), 5207–5216.
- Hanks, T. C., & Kanamori, H. (1979). A Moment Magnitude Scale. *Journal of Geophysical Research*, 84, 2348–2350.
- Hartzell, S. H. (1992). Site response estimation from earthquake data. *Bulletin of the Seismological Society of America*, 82, 2308–2327.
- Hartzell, S., Liu, P. C., & Mendoza, C. (1996). The 1994 Northridge, California, earthquake; investigation of rupture velocity, rise time, and high-frequency radiation. *Journal of Geophysical Research*, 101(9), 20091–20108.
- Husid, P. (1967). *Gravity effects on the earthquake response of yielding structures. Report of earthquake engineering research laboratory*. California Institute of Technology.
- Izutani, Y., & Kanamori, H. (2001). Scale dependence of seismic energy-to-moment ratio for strike-slip earthquakes in Japan. *Geophysical Research Letters*, 28, 4007–4010.
- Karimiparidari, S., Zaré, M., Memarian, H., & Kijko, A. (2013). Iranian earthquakes, a uniform catalog with moment magnitudes. *Journal of Seismology*, 17(3), 897–911.
- Kinoshita, S. H. (1994). Frequency-Dependent Attenuation of Shear Waves in the Crust of the Southern Kanto Area, Japan. *Bulletin of the Seismological Society of America*, 84, 1387–1396.

- Konno, K., & Ohmachi, T. (1998). Ground-motion characteristics estimated from spectral ratio between horizontal and vertical components of microtremor. *Bulletin of the Seismological Society of America*, 88, 228–241.
- Lermo, J., & Chavez-Garcia, F. (1993). Site effect evaluation using spectral ratios with only one station. *Bulletin of the Seismological Society of America*, 83, 1574–1594.
- Menke, W. (1989). Geophysical data analysis: discrete inverse theory. In R. Dmowska & J. R. Holton (Eds.), *Int Geophys Series* (Vol. 45, p. 289). Academic Press.
- Mousavi-bafrouei, S. H., Mirzaei, N., & Shabani, E. (2014). A declustered earthquake catalog for the Iranian Plateau. *Annals of Geophysics*, 57(6), 1–25.
- Oth, A., Bindi, D., Parolai, S., & Di Giacomo, D. (2011). Spectral analysis of k-NET and kik-net data in Japan, Part II: On attenuation characteristics, source spectra, and site response of borehole and surface stations. *Bulletin of the Seismological Society of America*, 101, 667–687.
- Oth, A., Bindi, D., Parolai, S., & Wenzel, F. (2008). S-Wave attenuation characteristics beneath the Veranca region in Romania: New insights from the inversion of ground-motion spectra. *Bulletin of the Seismological Society of America*, 98, 2482–2497.
- Parolai, S., Bindi, D., & Augliera, P. (2000). Application of the generalized inversion technique (GIT) to a microzonation study: Numerical simulations and comparison with different site-estimation techniques. *Bulletin of the Seismological Society of America*, 90, 286–297.
- Parolai, S., Bormann, P., & Milkereit, C. (2001). Assessment of the natural frequency of the sedimentary cover in the Cologne area (Germany) using noise measurements. *Journal of Earthquake Engineering*, 5, 541–564.
- Salazar, W., Sardina, V., & Cortina, J. (2007). A hybrid inversion technique for the evaluation of source, path, and site effects employing S-wave spectra for subduction and upper-crustal earthquakes in El Salvador. *Bulletin of the Seismological Society of America*, 97, 208–221.
- Shahvar, M. P., Zare, M., & Castellaro, S. (2013). A unified seismic catalog for the Iranian plateau (1900–2011). *Seismological Research Letters*, 84, 233–249.
- Snyder, D. B., & Barazangi, M. (1986). Deep crustal structure and flexure of the Arabian Plate beneath the Zagros Collisional Mountain belt as inferred from gravity observations. *Tectonics*, 5, 361–373.
- Tchalenko, J. S., & Braud, J. (1974). Seismicity and structure of the Zagros (Iran): The Main Recent Fault between 33° and 35° N. *Philosophical Transactions of the Royal Society of London*, 277, 1–25.
- Wang, H., Ren, Y., & Wen, R. (2018). Source parameters, path attenuation and site effects from strong-motion recordings of the Wenchuan aftershocks (2008–2013) using a non-parametric generalized inversion technique. *Geophysical Journal International*, 212, 872–890.
- Zafarani, H., Hassani, B., & Ansari, A. (2012). Estimation of earthquake parameters in the Alborz seismic zone, Iran using generalized inversion method. *Soil Dynamics and Earthquake Engineering*, 42, 197–218.
- Zare, M., Amini, H., Yazdi, P., Sesetyan, K., Demircioglu, M. B., Kalafat, D., Erdik, M., Giardini, D., Asifkhan, M., & Tsereteli, N. (2014). Recent developments of the middle east catalog. *Journal of Seismology*, 18, 749–772.